Chapter 4

Collapse of clouds

The challenge of star formation lies in the vast change of density and temperature that distinguishes molecular clouds — the matter from which the stars form — and the star itself. To form a star, we need to achieve an increase in density by 20 orders of magnitude and in temperature by 6 orders of magnitude. This is only possible through the self-gravitational collapse of matter.

4.1 Spectral Energy Distributions (SEDs)

At this point, we introduce the concept of spectral energy distributions (SEDs). Star formation and especially the earliest collapse phases can often only be studied photometrically or at very low spectral resolution ($R < 10$). Detailed line profiles and/or velocity maps are often not available and hence continuum radiation provides the only clue to the nature of the young protostellar phases. Observing the star forming regions in multiple photometric bands ranging from the ultraviolet (U-band) to infrared and even sub-mm wavelengths allows us to reconstruct the total luminosity of dense cores, young stellar objects and protoplanetary disks.

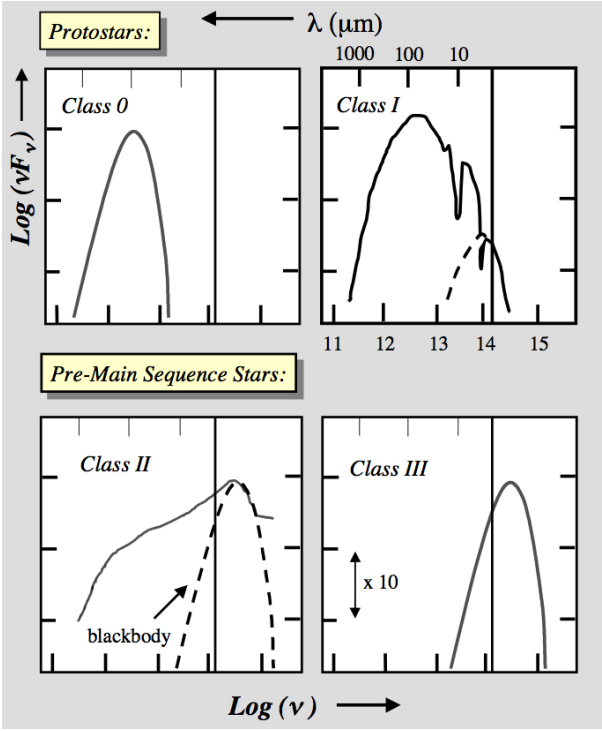

Figure 4.1: The empirical classification scheme for YSO spectral energy distributions. A vertical line appears at a wavelength of 2.2 μm for fiducial reference in each panel. Class 0 and Class III sources have distributions whose widths are similar to single temperature blackbody functions. Class II and Class I sources display infrared excess which produces energy distributions which are broader than a single blackbody function (from Lada 1999).

4.1.1 Lada classification

The shape of this energy distribution is closely related to the physical structure of the various objects. Embedded cores for example show a single-peak energy distribution that can be approximated by a single temperture black-body (Fig. 4.1). This is due to the optically thick nature of these objects where all received radiation has been re-processed by the gas and dust of the envelope. A star+disk system in later evolutionary phases displays a clear double peak

Table 4.1: Table with flux conversions.

To → **From ↓**	S_ν Jy	F_ν erg/cm^2/s/Hz	F_λ erg/cm^2/s/Å	f_E erg/cm^2/s/eV	f_λ erg/cm^2/s/Å
S_ν	$\boldsymbol{S}_\nu$	$10^{-23} S_n u$	$3.00 \times 10^{-5} S_n u/\lambda^2$	$1.51 \times 10^3 S_\nu/E$	$1.51 \times 10^3 S_\nu/\lambda$
F_ν	$10^{23}\ F_\nu$	$\boldsymbol{F}_\nu$	$3.00 \times 10^{18} F_\nu/\lambda^2$	$1.51 \times 10^{26} F_\nu/E$	$1.51 \times 10^{26} F_\nu/\lambda$
F_λ	$3.34 \times 10^4 \lambda^2 F_\lambda$	$3.34 \times 10^{-19} \lambda^2 F_\lambda$	$\boldsymbol{F}_\lambda$	$4.06 \times 10^6 \lambda^3 F_\nu$	$5.03 \times 10^7 \lambda F_\lambda$
f_E	$6.63 \times 10^{-4} E f_\mathrm{E}$	$6.63 \times 10^{-27} E f_\mathrm{E}$	$1.29 \times 10^{-10} E^3 f_\mathrm{E}$	$\boldsymbol{f}_\mathrm{E}$	$8.07 \times 10^{-2} E^2 f_\mathrm{E}$
f_λ	$6.63 \times 10^4 \lambda F_\lambda$	$6.63 \times 10^{-27} \lambda F_\lambda$	$1.99 \times 10^{-8} f_\lambda/\lambda$	$8.07 \times 10^{-2} \lambda^2 f_\lambda$	$\boldsymbol{f}_\lambda$

structure, with the stellar black-body peaking at optical wavelength and the cooler protoplanetary disk at infrared wavelengths (see also Fig. 1.16 in chapter 1). The stellar emission is still partly re-absorbed and scattered by the surrounding circumstellar material (disk and possibly envelope), causing veiling of the star in the UV. The energy removed in this way is reprocessed by the gas and dust in the envelope and re-emitted in the IR.

4.1.2 Characterization

Generally, the SED is shown as the energy density νF_ν or λF_λ emitted as a function of frequency ν or wavelength λ. Here, the units can differ vastly and all combinations of units are possible in the literature, leading to significant confusion and making the comparison of results often difficult to impossible. Table 4.1 shows examples of some of the most frequently used units and their conversion factors.

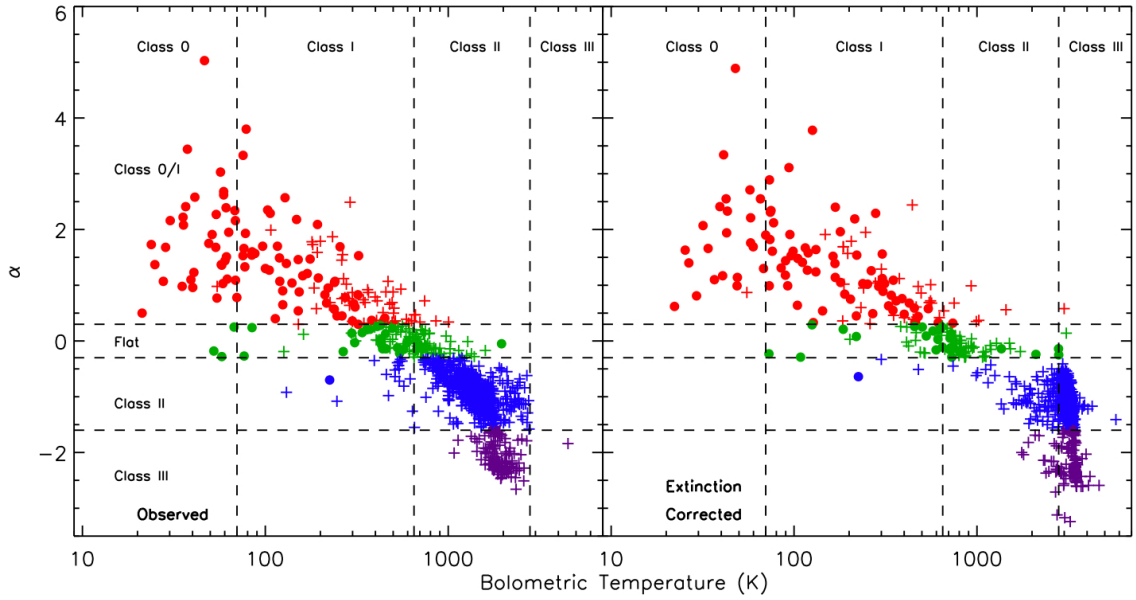

Figure 4.2: The value of α is plotted versus T_bol for each source with well-determined values. The color code is based on the Lada class of each source, as dened by α, with Class I plotted as red, flat as green, Class II as blue, and Class III as purple. Filled circles indicate sources associated with envelopes as traced by millimeter continuum emission, while plus signs indicate sources with no such associations. The right panel shows α' and T'_bol calculated after corrections for extinction were applied. The vertical dashed lines show the boundaries between classes, as defined by Chen et al. (1995). Figure and caption taken from Evans (2009).

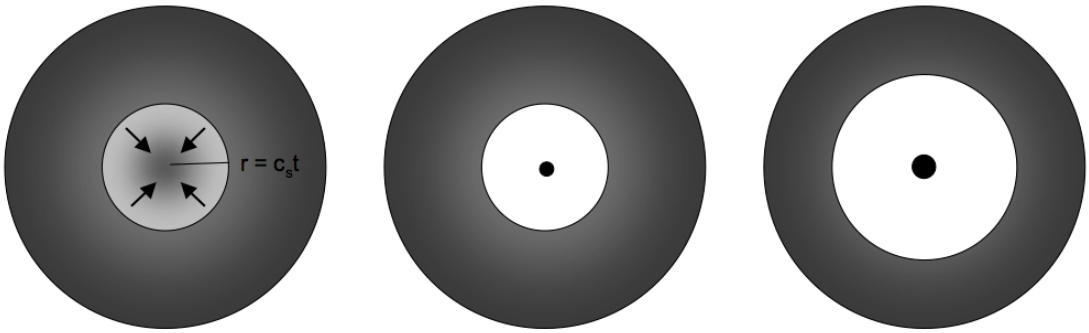

Figure 4.3: Sketch of the inside-out collapse scenario. The expansion wave travels outwards at a speed c_s.

Generally, an IR slope parameter $\alpha_{\rm IR}$ is defined as

$$\alpha_{\rm IR} = -\frac{d(\nu F_\nu)}{d\nu} \ , \tag{4.1}$$

in the wavelength region between 2.2 μm and several 10 μm. Typical values for $\alpha_{\rm IR}$ are larger than 0 for Class I objects, $-2 < \alpha_{\rm IR} < 0$ for Class II sources and < -2 for Class III sources. Another way of classifying young stellar objects (YSOs) is by their "bolometric temperature" which is the temperature of a black body with the same mean frequency as the SED of the YSO. Fig. 4.2 shows the results from the Spitzer Legacy Program c2d (Cores to Disks, PI: Evans). The statistics, i.e. the number of objects in each class, give an indication of the duration of the different phases of pre-main-sequence evolution. The extinction corrected estimated median lifetimes (or half-times) of Class 0 and I are 0.1, 0.44 Myr, respectively.

With the recent advent of large amounts of Spitzer SEDs, the onset of the IR excess $\nu_{\rm onset}$ (or $\lambda_{\rm onset}$) is used as a second parameter. It is defined as the wavelength where the measured fluxes start to be larger than the pure photospheric value. This parameter proved extremely useful in subclassifying the rather inhomegenous Class II sources, star+disk systems. We come back to this later when we discuss the observational appearance of protoplanetary disks in Chapter 11.

4.2 Shu inside-out collapse

The hydrodynamical collapse of a non-isotropic sphere is highly non-homologous. The central parts of a gravitationally unstable sphere collapse faster than the outer parts. If we assume that the central parts of the core have higher densities than the outer parts, the free-fall time $t_{\rm ff}$, which scales with $\rho^{-1/2}$, decreases towards the center. This means that the central parts collapse faster than the outer parts and the outer shells subsequently loose their pressure support, while the mass and hence the gravitational attraction inside such a shell does not change. The information of the 'lost pressure support' travels outwards as a wave with the sound speed c_s.

Frank Shu developed in his seminal paper from 1977 the so-called 'inside-out' collapse scenario and a self-similar dimensionless solution to the problem. Later numerical hydrodynamical simulations confirmed mainly four distinct phases:

1. **Free-fall phase:** The collapse is approximately isothermal and the timescale is the free-fall timescale. Efficient cooling is provided by molecular hydrogen and thermal radiation from dust grains (IR). The next two phase are adiabatic collapse phases, because the inner parts of the core becomes optically thick and thus cannot cool as efficient any more.

2. **First core phase:** The first stable core of a few AU in size forms. At temperatures in excess of 1000 K, dust grains evaporate removing them as an opacity source. Once the temperature reaches 2000 K, molecular hydrogen dissociates and a second collapse phase starts. This is because the equation

of state changes (adiabatic exponent) and thus gravity cannot be counterbalanced any more by the internal pressure.

3. **Opacity phase:** The second collapse is halted once the density is high enough ($> 10^{-2}$ g cm^{-3}) to provide a significant hydrogen ionization fraction, which changes the equation of state once again to a more favorite adiabatic exponent. Several more collapse phases can follow corresponding to the ionization of He and more massive atoms. At the end of phase 3, we are left with a core mass of ~ 0.01 M$_\odot$.

4. **Accretion phase:** The last phase is characterized by the entire core being optically thick and overall accretion. In this last phase, the protoplanetary disk forms. Actually, most of the material is accreted onto the star through this disk in the late collapse phase. It is also in this phase that the protostar becomes first visible in the infrared. Low mass stars ($M_{\rm Star} < 2$ M$_\odot$) finish their accretion and thus become exposed before they reach the main-sequence. They continue then to contract until their central temperature becomes high enough for hydrogen burning to start. More massive stars often reach the hydrogen burning limit and thus the main-sequence before the accretion phase ends.

4.2.1 Hydrodynamical equations

The basic hydrodynamical equations describing a collapsing dark core are

$$\text{Mass conservation}: \quad \frac{\partial M_r}{\partial t} + u\frac{\partial M_r}{\partial r} = 0, \quad \frac{\partial M_r}{\partial r} = 4\pi r^2 \rho \tag{4.2}$$

$$\text{Momentum conservation}: \quad \frac{\partial u}{\partial t} + u\frac{\partial u}{\partial r} = -\frac{c_s^2}{\rho}\frac{\partial \rho}{\partial r} - \frac{GM_r}{r^2} \tag{4.3}$$

$$\text{Energy equation}: \quad \frac{\partial L_r}{\partial M_r} = -\frac{\partial U_{\rm in}}{\partial t} - P\frac{\partial(\rho^{-1})}{\partial t} \tag{4.4}$$

Here, r is the radial coordinate, M_r the mass inside a radius r, u the infall velocity, c_s the sound speed, ρ the density, G the gravitational constant, L_r the total energy flux through the surface that includes the mass M_r, and $U_{\rm in}$ the internal energy. The energy flow through the surface can be derived from the basic concepts of energy transport through radiation (see e.g. Kutner, chapter 9.4.2)

$$L_r = \frac{16\pi\sigma_{\rm SB} r^2 T^3}{3\kappa_R}\frac{\partial T}{\partial r} \ , \tag{4.5}$$

where κ_R is the Rosseland mean opacity (gives the fraction of radiation absorbed per cm), and $\sigma_{\rm SB}$ the Stefan-Boltzmann constant.

Following Shu (1977), we can understand the inside-out collapse also as an outward traveling expansion wave (see Fig. 4.3). If we now define a new variable that travels with the expansion wave,

$$x = \frac{r}{c_s t} \ , \tag{4.6}$$

we can make the following 'Ansatz' for the density, mass and velocity solution using the 'to be determined' functions $\alpha(x), m(x)$ and $v(x)$

$$\rho(r,t) = \frac{\alpha(x)}{4\pi G t^2}, \qquad M_r = \frac{c_s^3 t}{G} m(x), \qquad u(r,t) = c_s v(x) \tag{4.7}$$

You can find the details of the derivation of these functions in the original paper by Shu. Fig. 4.4 shows the time evolution of the collapse until the expansion wave reaches the initial outer boundary. The inner part of the density profile is determined by the free-fall collapse. For $x \ll 1$, hence $r \ll c_s t$, the density and velocity in the free-fall region can be described as

$$\rho(r,t) = \frac{c_s^{3/2}}{17.96\, G}\frac{1}{\sqrt{t}}\frac{1}{r^{3/2}}, \qquad u(r,t) = \sqrt{\frac{2GM_*(t)}{r}} \ . \tag{4.8}$$

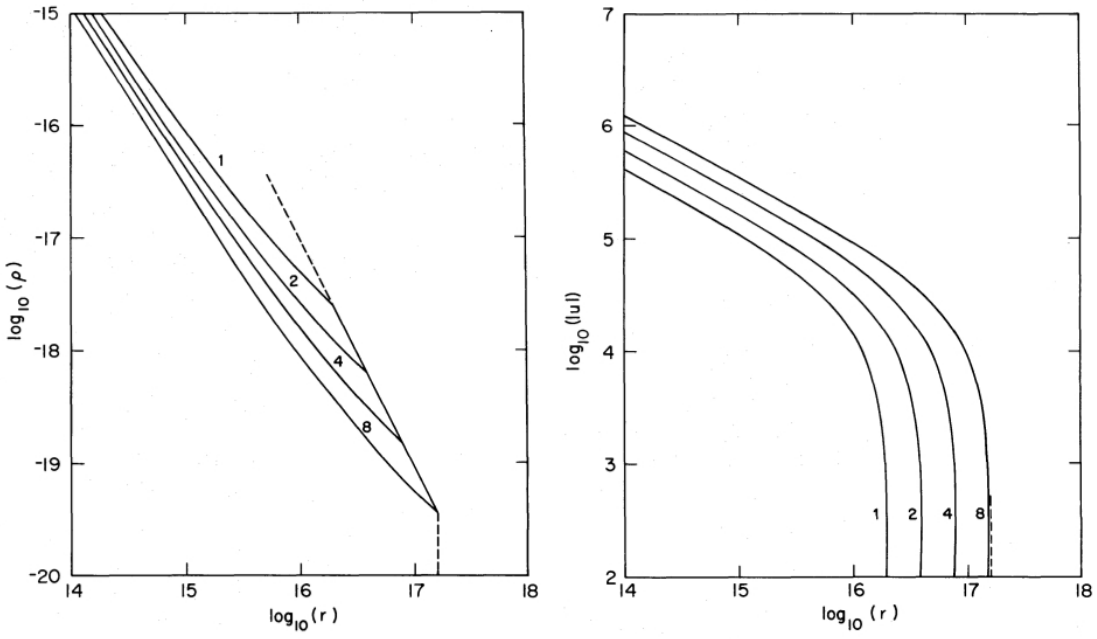

Figure 4.4: Left: Density as a function of radial coordinate for the inside-out collapse of a 0.96 $M_\odot$ core with an initial velocity of 0.2 km/s. The initial radius of the outer boundary is indicated by the dashed line. The different profiles correspond to $t = 1, 2, 4, 8 \times 10^{12}$ s $(3.2, 6.3, 12.7, 25.4 \times 10^4$ yr). Right: The corresponding velocity profiles. The plots are in cgs units.

The accretion rate $\dot{M} = \frac{\partial M_r(0,t)}{\partial t}$ follows from Eq.(4.7)

$$\dot{M} = 0.975 \frac{c_s^3}{G} \tag{4.9}$$

and is constant. This implies that the stellar mass grows linear with time.

As we move outwards in the solution, we encounter a transition region, where matter starts to fall towards the center. The kink in the profile indicates the position of the expansion wavefront (always at $x = 1$). Outside that point, we see an isothermal sphere solution with $\rho \sim r^{-2}$.

4.2.2 Instabilities

The adiabatic index Γ is used to describe the relation between the pressure P and the volume V of a gas during an adiabatic compression or expansion. For such a process, PV^Γ is a constant. This means that for a small adiabatic change in volume and pressure, we can write

$$\begin{aligned} \Gamma \frac{dV}{V} + \frac{dP}{P} &= 0 \\ V dP &= -\Gamma P dV \end{aligned} \tag{4.10}$$

and hence

$$\begin{aligned} d(PV) &= P dV + V dP \\ &= -(\Gamma - 1) P dV \end{aligned} \tag{4.11}$$

During an adiabatic collapse, there is no heat transfer and so the change in internal energy $U_{\rm in}$ of the system can be written as

$$\mathrm{d}U_{\rm in} = -P\mathrm{d}V = \frac{1}{\Gamma - 1}\mathrm{d}(PV) \ . \tag{4.12}$$

Hence, for a constant adiabatic index Γ, the relation

$$U_{\rm in} = \frac{1}{\Gamma - 1}PV \tag{4.13}$$

holds. For a system in virial equilibrium, the average pressure $< P >$ can be written as one third of the density of stored gravitational energy

$$< P >= -\frac{1}{3}\frac{U_{\rm G}}{V} \ . \tag{4.14}$$

For a self-gravitating gas in hydrostatic equilibrium, we can thus write

$$\begin{aligned} -\frac{1}{3}\frac{U_{\rm G}}{V} &= (\Gamma - 1)\frac{U_{\rm in}}{V} \\ 3(\Gamma - 1)U_{\rm in} + U_{\rm G} &= 0 \end{aligned} \tag{4.15}$$

The total energy is

$$U_{\rm tot} = U_{\rm in} + U_{\rm G} = (4 - 3\Gamma)U_{\rm in} \ , \tag{4.16}$$

and the system is bound or stable if $U_{\rm tot} < 0$, hence if $\Gamma > 4/3$.

On the other hand, Eq.(4.5) indicates that $\Gamma < 5/3$. This is the limit for radiative energy transport. If Γ were larger, the system would become instable to convection and energy transport could happen that way as well.

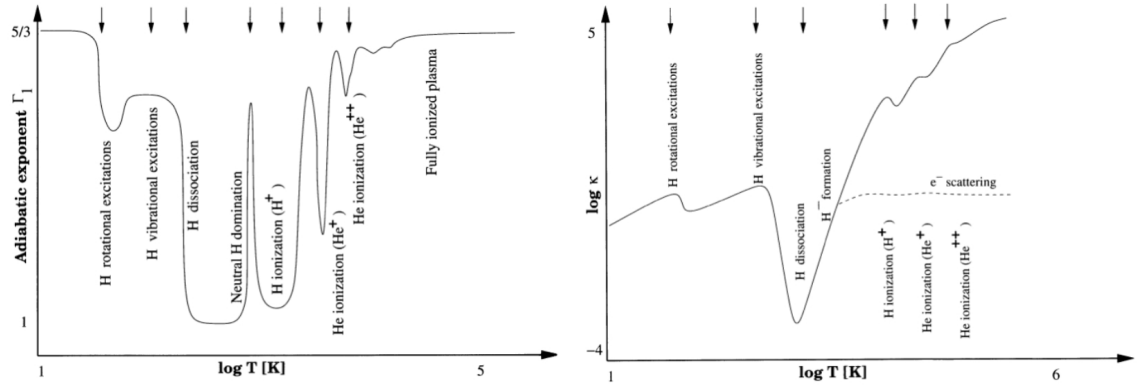

Figure 4.5: Left: The adiabatic index (Γ_1 is called the first adiabatic index, $\left(\frac{\partial \ln P}{\partial \ln \rho}\right)_{\rm ad}$) as a function of temperature. The arrows mark the onset of specific physical processes that change the index most dramatically causing instability in the nearly formed stellar core (figure and caption from Schulz 2005). Right: The Rosseland mean opacity κ_R as a function of temperature taken from the same calculation as the adiabatic index. It shows the behaviour of opacity parallel to the changes in the adiabatic index and thus how it can counter drifts into instability regions (figure and caption from Schulz 2005). Comment: The leftmost three arrows should be labelled with H_2 instead of H.

Fig. 4.5 shows on the left the adiabatic index as a function of temperature T. With increasing temperature, the molecules in the gas get first excited, and then they dissociate (H_2 at ~ 2000 K[1]). Above a critical temperature, which is density dependent, the gas becomes more and more ionized. The figure was computed for a gas density of 10^{-14} g cm^{-3}. With changing density, the depth and heights of these peaks and valleys in Γ changes.

[1]Under conditions of thermodynamic equilibrium, the dissociation constant $K(\mathrm{H}_2)$ is related to the partial pressure of the atomic constituent $p(\mathrm{H})$ and $p(\mathrm{H}_2)$ through $K(\mathrm{H}_2) = p^2(\mathrm{H})/p(\mathrm{H}_2)$. The dissociation constant K depends only on temperature. At 2000 K, $K(\mathrm{H}_2) = 3.45$ dyn/cm^2.

4.2.3 Opacities

The right side of Fig. 4.5 shows the gas opacities as a function of temperature T corresponding to the change in adiabatic index shown in the left side of Fig. 4.5. The opacity is needed to prevent too much energy from leaking out. This enables the temperature and thus the pressure in the core to build up and hence hydrostatic equilibrium to be established. To calculate the Rosseland mean opacity for a certain gas mixture, we need to know the individual opacities for more than 60 million atomic, molecular transitions from neutral and ionized stages. This has largely been enabled by the nuclear bomb experiments after the second world war. Later astrophysics benefitted from this data and the largest projects were the Opacity Project (OP) and the Opacity Project at Livermore (OPAL).

The Rosseland opacity shown here contains also grain opacities at low temperature (typical condensation temperatures of grains are around 1300 K). At low temperatures and densities, changes in the opacity are due to the melting of grains ice mantles and later grain evaporation. The next changes arise from the ionization of alkali metals and then the dissociation of H_2.

Instabilities that are caused by rapid changes in opacity in connection with increasing temperature and density are called 'secular' instabilities. If κ_R increases upon adiabatic compression, we call these instabilities 'vibrational' instabilities. They are more complex than the dynamical instability that arises from the adiabatic index only.

4.2.4 Rotating collapse

The previously sketched picture of a spherical inside-out collapse (gravity versus pressure) cannot explain a series of observational phenomena that accompany star formation. These are for example the presence of protoplanetary disks, jets and outflows. While magnetic fields or rotation will not prevent the collapse, they will change the way matter flows and accretes.

We now briefly consider the impact of rotation on the protostellar collapse. Since the cloud remains hydrodynamical stable for a long time, we can assume that it rotates as a solid body. Also, we assume that the cloud rotates slowly, so that the centrifugal force is initially very small and the early stages of collapse are almost radial. In this limit, we can distinguish between an outer envelope which stays almost spherical and an inner region that gets distorted due to rotation and forms an equatorial accretion disk (Fig. 4.6).

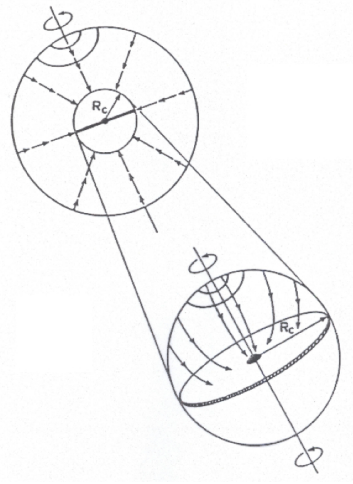

Figure 4.6: Sketch of an inside-out collapse including rotation. The outer envelope stays spherical and the inner region is affected by the rotation. The radius dividing these two zones is the centrifugal radius r_c (or here denoted as R_c). Inside the centrifugal radius, an equatorial accretion disk forms.

Depending on the specific angular momentum of a gas parcel, it will either be able to accrete onto the protostellar core (very low specific angular momentum) or accrete onto the equatorial disk at some radius corresponding to its specific angular momentum. The maximum possible distance from the star at which such a gas parcel can end up is called the centrifugal radius r_c. This is also the quantity limiting the inner region and thus the size of the accretion disk. In the following paragraphs we will derive this quantity from simple principles.

If we study the trajectory of a fluid element during the infall, we can assume that the protostar + disk mass is a point source and that the only gravity and rotation play a role. Under these circumstances, the fluid element will have a bound elliptical orbit (the conic section corresponding to a negative energy — hence an ellipse or circle; unbound orbits have conic sections corresponding to a parabola or hyperbola). However,

since the inital energy is small compared to the energy it has when it reaches the equatorial plane, we can approximate it reasonably well by a parabola (zero-energy or unbound orbit; parabola open to the left — along x-axis — focus at (0,0))

$$r = \frac{r_{\rm eq}}{1+\cos\Psi} \ , \tag{4.17}$$

where the coordinates and quantities are introduced in Fig. 4.7. If the fluid element would reach $r_{\rm min}$, the maximum orbital velocity would be

$$v_{\rm max}^2 = \frac{2GM_*}{r_{\rm min}} \ , \tag{4.18}$$

where M_* is the mass of the protostar + disk. However, the fluid element will never reach that part of the trajectory since it collides with the forming disk at $\Psi = 90^{\rm o}$. The specific angular momentum can be written as

$$j^2 = r_{\rm min}^2 v_{\rm max}^2 = 2GM_* r_{\rm min} \ . \tag{4.19}$$

Since the fluid element reaches $r_{\rm min}$ at $\Psi = 0$, Eq.(4.17) implies that $r_{\rm min} = r_c/2$. Therefore, we can write the radius at which the fluid element reaches the plane as

$$r_{\rm eq} = \frac{j^2}{GM_*} \ . \tag{4.20}$$

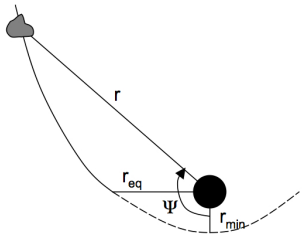

Figure 4.7: Sketch of a parabolic orbit in rotating infall. A fluid element with polar coordinates (r, Ψ) falls in and hits the equatorial disk at a radius $r_{\rm eq}$. In the absence of the disk, the fluid element would have reached the smaller distance $r_{\rm min}$ before swinging back out again.

Now we can express the specific angular momentum in terms of the initial quantities Ω_0 (angular velocity) and θ_0 (inclination of orbital plane with respect to the rotation axis, $\theta_0 = 90^{\rm o}$ is the midplane)

$$j = R^2\Omega_0 \sin\theta_0 = c_s^2 t^2 \Omega_0 \sin\theta_0 \ , \tag{4.21}$$

where R is the distance from the center at which the fluid element starts its collapse (position of the rarefaction wave at time t — its speed is c_s and hence $R = c_s t$). The angular momentum is larger for higher values of θ_0 and has a maximum at $\theta_0 = 90^{\rm o}$ (the centrifugal radius). Inserting this into Eq.(4.20) and using the expression found for the core mass $M_r(t)$ in Sect. 4.2.1, we can rewrite $r_{\rm eq}$ as

$$r_{\rm eq} = \frac{c_s t^3 \Omega_0^2 \sin\theta_0^2}{m_0} \ . \tag{4.22}$$

For $\theta_0 = 90^{\rm o}$, $r_{\rm eq}$ is the centrifugal radius of the disk

$$r_c \approx 7.33 \text{ AU} \left(\frac{c_s}{0.35 \text{ km/s}}\right) \left(\frac{\Omega}{10^{-14} \text{ s}^{-1}}\right)^2 \left(\frac{t}{10^5 \text{ yr}}\right)^3 \ . \tag{4.23}$$

For the latter expression, we assumed that $m_0 \sim 1$ (see Sect. 4.2.1). The value $\Omega = 10^{-14}$ s^{-1} is close to typical observed values of a few times 10^{-14} - 10^{-13} s^{-1}. This gives us also an estimate of the initial size of the accretion disk. We will later see that the size of this initial disk grows in the later stages of star formation due to e.g. angular momentum transport (viscous spreading of the disk).

4.2.5 Collapse in the presence of a magnetic field

An additional complexity is introduced by the presence of a magnetic field. Typical values in molecular clouds are small, of the order of a few 10 μG. We consider here for simplicity the non-rotating case. The magnetic field causes an additional pressure component that can counterbalance the collapse of the core. In the case of a poloidal magnetic field (Fig. 4.8), the outward moving expansion wave (Sect. 4.2.1) travels

faster parallel to the magnetic field lines. Even though the gas flow itself slows down in the presence of a magnetic field, the expansion wave travels faster, resulting in an almost unchanged mass accretion rate $\dot{M}$.

In analogy to the previous section, we can now define a magnetic centrifugal radius

$$r_b = k_b G^{2/3} B_0^{4/3} c_s^{-1/3} t^{7/3} \tag{4.24}$$

$$\approx 540 \text{ AU} \left(\frac{B_0}{30\ \mu\text{G}}\right)^{4/3} \left(\frac{c_s}{0.35 \text{ km/s}}\right)^{-1/3} \left(\frac{t}{10^5 \text{ yr}}\right)^{7/3} , \tag{4.25}$$

where $k_b = 0.12$ (from numerical calculations). Typically, r_b is 1-2 orders of magnitude larger than r_c. Fig. 4.9 illustrates the collapse environment roughly 2×10^5 yr after the onset of collapse (left) and at the end of the free-fall phase (right). This figure illustrates the formation of a pseudo-disk (caused by magnetic forces deflecting the infalling gas towards the equatorial plane) that has in the end a size of ~ 1000 AU. We can picture the much smaller centrifugally supported disk inside the thick line (labelled 'inside solution'). Hence, we can imagine that the inner accretion disk is fed by the outer magnetically stabilized pseudo-disk.

Another characteristic scale is the radius r_m at which magnetic and thermal pressure are equal

$$\frac{B_0^2}{8\pi} \sim \rho c_s^2 \ . \tag{4.26}$$

At the begin of the collapse, we can approximate the density profile as that of an isothermal sphere (see Sect. 4.2.1)

$$\rho = \frac{c_2^2}{2\pi G r^2} \ . \tag{4.27}$$

Inserting this in Eq.(4.26) yields

$$\frac{B_0^2}{8\pi} = \frac{c_s^4}{2\pi G r^2} \tag{4.28}$$

$$r_m = \frac{2c_s^2}{B_0\sqrt{G}} \ . \tag{4.29}$$

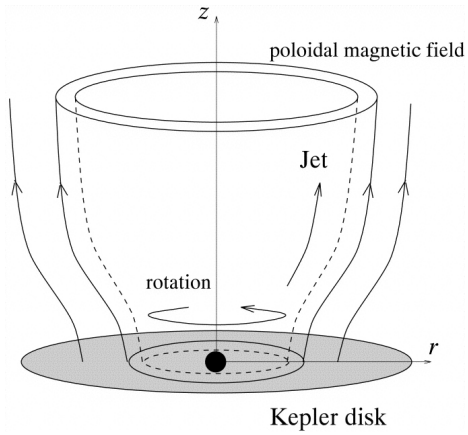

Figure 4.8: Sketch of the poloidal magnetic field during the protostellar collapse.

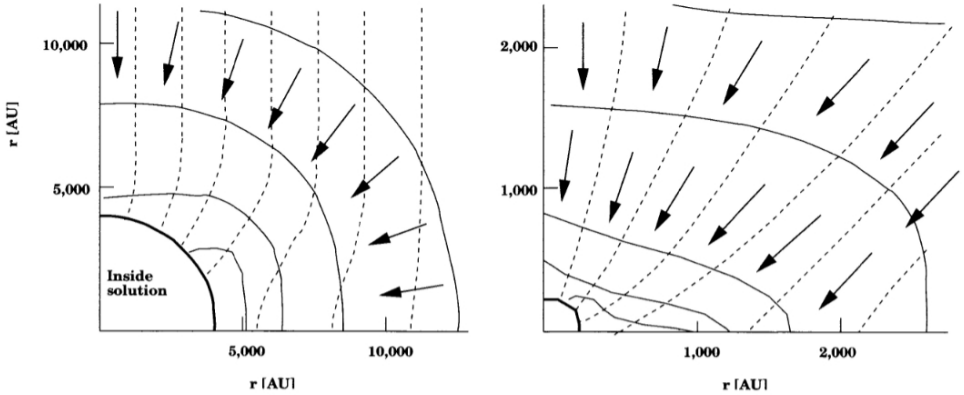

Figure 4.9: Illustration of a collapse of a magnetic spherical, isothermal sphere at about 2×10^5 yr (left) and at the end of the free-fall phase (right). The solid lines are contours of equal density, the dashed lines are magnetic field lines, the thick arrows show the velocity field. The horizontal and vertical axis are in AU.

4.3 Line profiles

If spectrally resolved, line profiles carry information on the gas motion along the line of sight, its absolute values and signs. The characteristic emission profile of the protostellar collapse phase is an asymmetric double-peaked line. We can understand the formation of this profile from a simple sketch of the radial density and temperature profile of the core and its velocity structure. For that, Fig. 4.10 illustrates how the profile is composed if we assume that the collapse can be approximated by a series of uniform gas density and temperature shells. The central shells have higher densities and temperatures compared to the outer shells (see top panel). The layers in front of the protostar produce redshifted emission, while the ones behind the protostar produce blueshifted emission (the red and blue arrows indicate the infall motion of the shells - middle panel). An important pre-requisite for observing such a collapse signature is that the line is optically thick. An optically thin line is symmetric and thus indistinguishable from a normal emission line without infall/outflow. The line profile can be broken up into velocity bins corresponding to the individual layers. The layer responsible for most of the emission in a velocity bin is indicated by its number. The degree of radiation leaking into neighboring velocity bins is given by the turbulent velocity field (σ). If the line is optically thick, absorption turns the line profile asymmetric as outer cooler gas shells in the redshifted wing can partially absorb emission from the hotter shells that are closer to the protostar. This is not the case for the blueshifted wing, because in that case, the gas temperature increases towards the observer (hotter inner shells are closer to us than the cool outer shells). In the optically thin case, we do not encounter absorption and hence the profile stays symmetric.

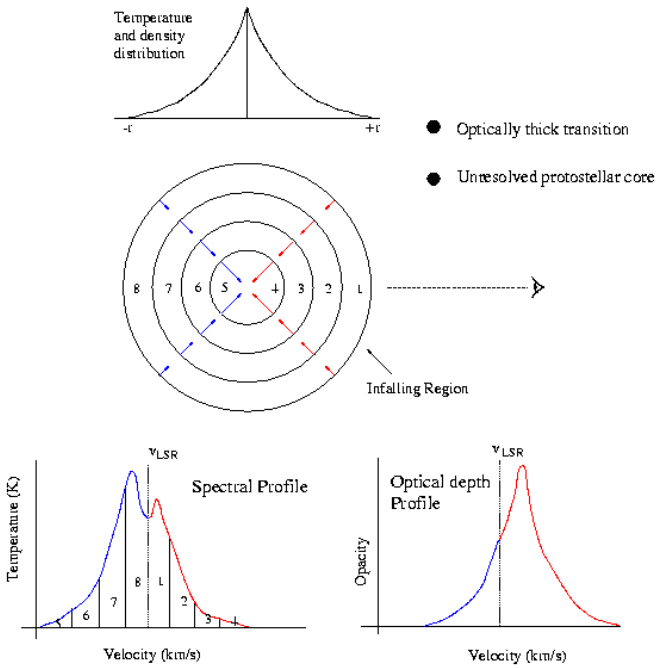

Figure 4.10: Sketch of the line profile formation in a collapsing core.

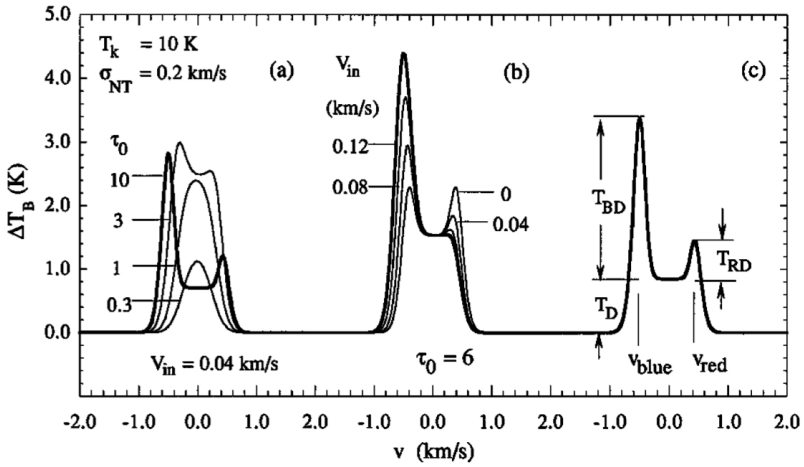

Figure 4.11: Variation of infall asymmetry (a) with peak optical depth τ_0 and (b) with infall speed $V_{\rm in}$ (from Myers et al. 1996). (c) illustrates the definition of various line parameters.

Fig. 4.11 illustrates this for a series of models with varying optical depth and infall velocities. In a radiative transfer model of two uniform layers with velocity dispersion σ and approach speed $V_{\rm in}$, the line profile is symmetric for $\tau_0 < 1$, but its peak skews to the blue as τ increases beyond 1. For $V_{\rm in} < \sigma$ and increasing τ_0, the profile has two peaks, with increasing ratio of blue to red peak intensity. As $V_{\rm in}$ increases for fixed $\tau_0 > 1$, the blue-red intensity ratio increases until the red peak disappears into a red shoulder. The right panel of Fig. 4.11 illustrates the definition of a set of line parameters used to estimate the infall speed from the line profile

$$V_{\rm in} \approx \frac{\sigma^2}{v_{\rm red} - v_{\rm blue}} \ln\left(\frac{1 + eT_{\rm BD}/T_{\rm D}}{1 + eT_{\rm RD}/T_{\rm D}}\right) \qquad (4.30)$$

The infall line asymmetry is not limited to the central velocities. The asymmetry can occur in the line wings as long as the emission stays optically thick.

Fig. 4.12 illustrates the infall line profiles in the starless core L1544 (Trafalla et al. 1998). The lines vary from the high optical depth HCO^+ 1-0 line with strong infall asymmetry to the low optical depth $C^{34}S$ 2-1 line without infall asymmetry.

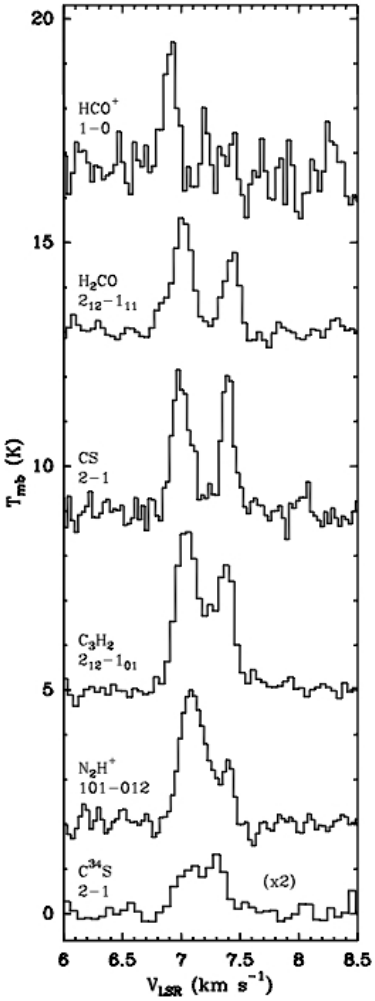

Figure 4.12: Spectral profiles of dense gas tracer lines in the starless core L1544 (Tafalla et al. 1998).